Nano Research

Open Access

Research Article

A three-dimensional tunnel ion sieve interface for ultra-long life Zn metal anodes

Baoliang Lu[1,2,3,4], Guixin Zhang[1,2,3,4], Yaxin Lu[1,2,3,4], Ling Wang[1,2,3,4], Yuxiang Zhou[1,2,3,4], Hongqiang Wang[1,2,3,4] ✉, Qingyu Li[1,2,3,4], and Zhaoling Ma[1,2,3,4] ✉

[1] *Guangxi Key Laboratory of Low Carbon Energy Materials, School of Chemistry and Pharmaceutical Sciences, Guangxi Normal University, Guilin 541004, China*
[2] *Guangxi New Energy Ship Battery Engineering Technology Research Center, School of Chemistry and Pharmaceutical Sciences, Guangxi Normal University, Guilin 541004, China*
[3] *Guangxi scientific and technological achievements transformation pilot research base of electrochemical energy materials and devices, School of Chemistry and Pharmaceutical Sciences, Guangxi Normal University, Guilin 541004, China*
[4] *University Engineering Research Center of Advanced Functional Materials and Intelligent Sensing, School of Chemistry and Pharmaceutical Sciences, Guangxi Normal University, Guilin 541004, China*

Cite this article: *Nano Research*, **2026**, *19*, 94908542. https://doi.org/10.26599/NR.2026.94908542

ABSTRACT: The stable Zn metal anode is pivotal for advancing aqueous Zn-ion batteries, yet it remains challenged by rampant dendrite growth and parasitic side reactions. Herein, the spinel structured ZnV_2O_4 with moderate oxygen vacancies serves as an ion-sieve interphase on the Zn anode, whose superior selectivity of tunnel size enables a high ionic conductivity up to 10.56 mS·cm^{-1}. The surface oxygen vacancies can promote the strong adsorption towards Zn ions and subsequent desolvation. The moderate oxygen vacancy content preserves the inner integrality of connectivity tunnels for ZnV_2O_4 interphase facilitating the rapid ion transport kinetics. COMSOL simulation and density functional theory (DFT) calculation conjointly confirm the higher Zn^{2+} flux and the accelerated desolvation kinetics. Consequently, equipped with ZnV_2O_4@Zn anode, the symmetric cell delivers an ultra-stable cycling lifespan exceeding 3700 h at 4 mA·cm^{-2}/1 mAh·cm^{-2}. Even at the condition of 8 mA·cm^{-2}/1 mAh·cm^{-2}, the symmetric cell maintains a stable cycling for over 900 h. This work underscores the critical factor of the compatibility of oxygen vacancy and ion sieve tunnel geometry, thereby paving a promising avenue for constructing durable aqueous Zn-ion batteries.

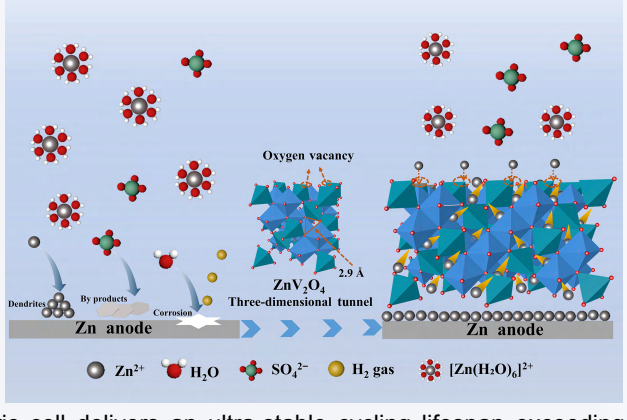

KEYWORDS: Zn-ion battery, Zn anode, ZnV_2O_4, three-dimensional tunnel, ion sieve

1 Introduction

Rechargeable aqueous Zn-ion batteries have great promise to meet the demand for large-scale energy storage due to Zn metal featuring high gravimetric and volumetric capacities (820 mAh·g^{-1} and 5854 mAh·cm^{-3}), low redox potential (−0.762 V versus the standard hydrogen electrode), abundant reserves, intrinsic safety, and environmental friendliness [1–8]. Nevertheless, the practical application of Zn metal anodes is still plagued by the generation of Zn dendrites and the hydrogen evolution related side reaction, along with the rapid capacity deterioration and unsatisfactory Coulombic efficiency (CE) [9–11]. Indeed, these aforementioned issues primarily originate from the unstable anode/electrolyte interface, which leads to a non-uniform Zn^{2+} flux distribution and consequently induces uncontrolled and irregular Zn dendrite growth. Meanwhile, parasitic side reactions between Zn metal and water molecules, accompanied by H_2 evolution, continuously consume both Zn and electrolyte, resulting in the accumulation of by-products $ZnSO_4·6H_2O$ [12–20] and ultimately causing premature battery failure [21, 22].

To strengthen the anode/electrolyte interface, an array of strategies has been developed, encompassing electrolyte

Received: December 2, 2025; **Revised:** January 28, 2026
Accepted: February 5, 2026

✉Address correspondence to Zhaoling Ma, zhaolingma@163.com; Hongqiang Wang, whq74@126.com

composition optimization, electrode architecture design, separator modification, and the construction of artificial electrode/electrolyte interface [23–31]. In the above strategy, a robust electrode/electrolyte artificial interface can regulate the directional uniform deposition of Zn^{2+} flux and obstruct the immediate contact of active water molecules with Zn metal. Various interface layer materials, such as carbon composites, metal alloys, metal oxides, and polymers, are utilized to protect Zn anode by the induction and barrier functionality [32–37]. Recently, ion-sieve material with ordered channels possesses high ion selectivity and excellent reactive water molecular peeling for Zn^{2+} electrochemical deposition [38]. Oxide-based ion sieve interphase layers are found to have abundant surface oxygen vacancies, which enhance zincophility, promote metal nucleation, and lower the desolvation barrier. Metal–organic framework (MOF) derived HfO_{2-x} artificial layer, by virtue of its structural porosity and surface oxygen vacancies, can achieve excellent cycling performance of over 5000 h at 1 mA·cm^{-2} [39]. A defect spinel structured $Zn_2Ti_3O_8$ protective layer with the induced oxygen vacancies gives outstanding cyclic lifetime of up to 1600 h at larger current density of 10 mA·cm^{-2} [40]. Fluorite structured CeO_2 aerogel interface layer exhibits a long-term lifespan over 4000 h at 4 mA·cm^{-2} and 1200 h under an ultrahigh 85% Zn utilization at 8 mA·cm^{-2} [41]. Although the fluorite structured sieve interface layers also possess the three-dimensional (3D) tunnels for ion transport, their target carried ions are mainly for the anions. Furthermore, the relationship between oxygen vacancy content and the ion transport rate of different tunnel geometries is still unexplored. The spinel-structured ion sieve interface layer with oxygen vacancies favors cation transport, which is beneficial for high Zn^{2+} flux, and the lower bottleneck size enables more effortless access for traversing the interface layer.

Herein, we propose a spinel structured ZnV_2O_4 ion sieve interface layer with surface oxygen vacancies and three-dimensional interconnected tunnels enabling ultrafast ion transport kinetics and lower desolvation barrier for the long stable Zn metal anodes. Due to the moderate surface oxygen vacancies, ZnV_2O_4 offers abundant zincophilic sites promoting the dendrite-free Zn electrode. Furthermore, with unique inner three-dimensional connectivity structure and the tunnel dimension of 2.8–3.0 Å, ZnV_2O_4 ion sieve interface layer can preferentially transport Zn^{2+} through the interconnected multipath due to the rational ion size of 1.48 Å for Zn^{2+}, and even achieve a superior ionic conductivity of 10.56 mS·cm^{-1}, which guarantees the outstanding rate performance. In symmetric ZnV_2O_4@Zn//ZnV_2O_4@Zn cell system, the Zn anode achieves an ultra-long lifespan exceeding 3700 h at 4 mA·cm^{-2}. Even at a large current density of 8 mA·cm^{-2}/1 mAh·cm^{-2}, the symmetric cell maintains a stable cycling for over 900 h. In full cell, ZnV_2O_4@Zn still demonstrates remarkably improved cycle durability of 1000 h at 1 A·g^{-1}.

2 Results and discussion

We synthesize the spinel structured ZnV_2O_4 through an easy to scale-up method of sol–gel process, coupling calcination at 700 °C [42]. X-ray diffraction (XRD) pattern in Fig. 1(a) confirms the spinel structure of ZnV_2O_4, consistent with PDF#75-0318. This structure is characterized by a cubic close-packed (ccp) lattice of oxygen anions (O^{2-}), in which Zn^{2+} cations occupy tetrahedral interstices to form [ZnO_4] units, while V^{3+} cations occupy octahedral sites, forming [VO_6] octahedra. The [VO_6] and [ZnO_4] polyhedra, interconnected via corner- and/or edge-sharing, give rise to a robust and open framework with well-defined interstitial tunnels, as shown in Fig. S1 in the Electronic Supplementary Material (ESM). Figure 1(b) shows the jujube-like morphology of ZnV_2O_4 with an average diameter of approximately 50 nm. The crystallinity of ZnV_2O_4 increases with increasing calcination temperature (Fig. S2 in the ESM), and this result is consistent with the observations from transmission electron microscopy (TEM) and high-resolution TEM (HRTEM) shown in Fig. S3 in the ESM. With the increased intrinsic crystallinity, the ionic conductivity of ZnV_2O_4 calcined at 700 °C (10.56 mS·cm^{-1}) is far more than that of ZnV_2O_4 calcined at 500 and 600 °C (Fig. 1(c) and Fig. S4 in the ESM). Consequently, the ZnV_2O_4 calcined at 700 °C is chosen as the ion sieve interface due to its fast ion transport. ZnV_2O_4@Zn electrodes are prepared by coating the slurry of ZnV_2O_4 on Zn foil. Side-view scanning electron microscopy (SEM) image and energy dispersive X-ray spectroscopy (EDX) mapping images show that an approximate 5 μm thickness of ZnV_2O_4 interphase is uniformly coated on Zn foil with 100 μm thickness (Fig. 1(d)). The contact angle test in Fig. 1(e) indicates that the ZnV_2O_4@Zn exhibits greater hydrophobicity than the bare Zn. Figure 1(f) presents the linear sweep voltammetry (LSV) curves of the ZnV_2O_4@Zn and bare Zn. ZnV_2O_4@Zn (−114 mA·cm^{-2}) shows a significantly lower current density at −1.5 V compared to the bare Zn (−205 mA·cm^{-2}), suggesting that the ZnV_2O_4@Zn effectively mitigates the hydrogen evolution reaction (HER). The corresponding Tafel slope results from Fig. S5 in the ESM also indicate that the ZnV_2O_4@Zn effectively reduces the HER rate, where the Tafel slope of 88.03 mV·dec^{-1} for the ZnV_2O_4@Zn is higher than that of bare Zn. The corrosion characteristics of the anodes were investigated through Tafel polarization test as presented in Fig. 1(g). The ZnV_2O_4@Zn electrode exhibits a corrosion current of 1.229 mA·cm^{-2}, lower than the 1.395 mA·cm^{-2} of bare Zn, demonstrating the superior corrosion protection capability.

To investigate the actual effect of suppressing by-products, the soaking experiment of ZnV_2O_4@Zn and bare Zn in 2 M $ZnSO_4$ is performed for 7 days. As illustrated in Fig. S6 in the ESM, the surface of ZnV_2O_4@Zn remains largely unchanged after the soaking test, while bare Zn shows the formation of white by-products. The corresponding XRD analysis in Fig. 1(h) confirms that the white by-products are $Zn_4SO_4(OH)_6{\cdot}5H_2O$. The top and side view SEM images of bare Zn and ZnV_2O_4@Zn anodes after soaking experiment reveal that there is a mass of by-products $Zn_4SO_4(OH)_6{\cdot}5H_2O$ on bare Zn relative to ZnV_2O_4@Zn (Figs. 1(i)–1(l)). To confirm the deposition location, we conducted Zn dissolution at a higher current density and subsequent Zn deposition at a lower current density at a depth of discharge (DOD) of 16%. Upon dissolution of the Zn anode, the released Zn^{2+} ions traverse the interfacial interphase to enter the bulk electrolyte, thereby creating a gap between ZnV_2O_4 interphase and Zn foil (Figs. 1(m) and 1(n) and Fig. S7 in the ESM). In terms of Zn ion deposition, Zn ions pass through and deposit beneath the ZnV_2O_4 interphase. As shown in Figs. S8–S10 in the ESM, the tunnels formed by the interconnected [ZnO_6] octahedra and [VO_4] tetrahedra exhibit the inner tunnel sizes in the range of 2.8–3.0 Å for ZnV_2O_4, and $[Zn(H_2O)_6]^{2+}$ hydrated ion and SO_4^{2-} anion possess an ionic size of approximately 5.58 and 4.8 Å, respectively [43–45]. Due to the smaller ion size of ~ 1.48 Å for the desolvated Zn^{2+}, the suitable tunnel sizes of ZnV_2O_4 interface layer can physically select for the easy access of Zn^{2+} after desolvation while hindering the migration of bulky SO_4^{2-} anions and hydrated species.

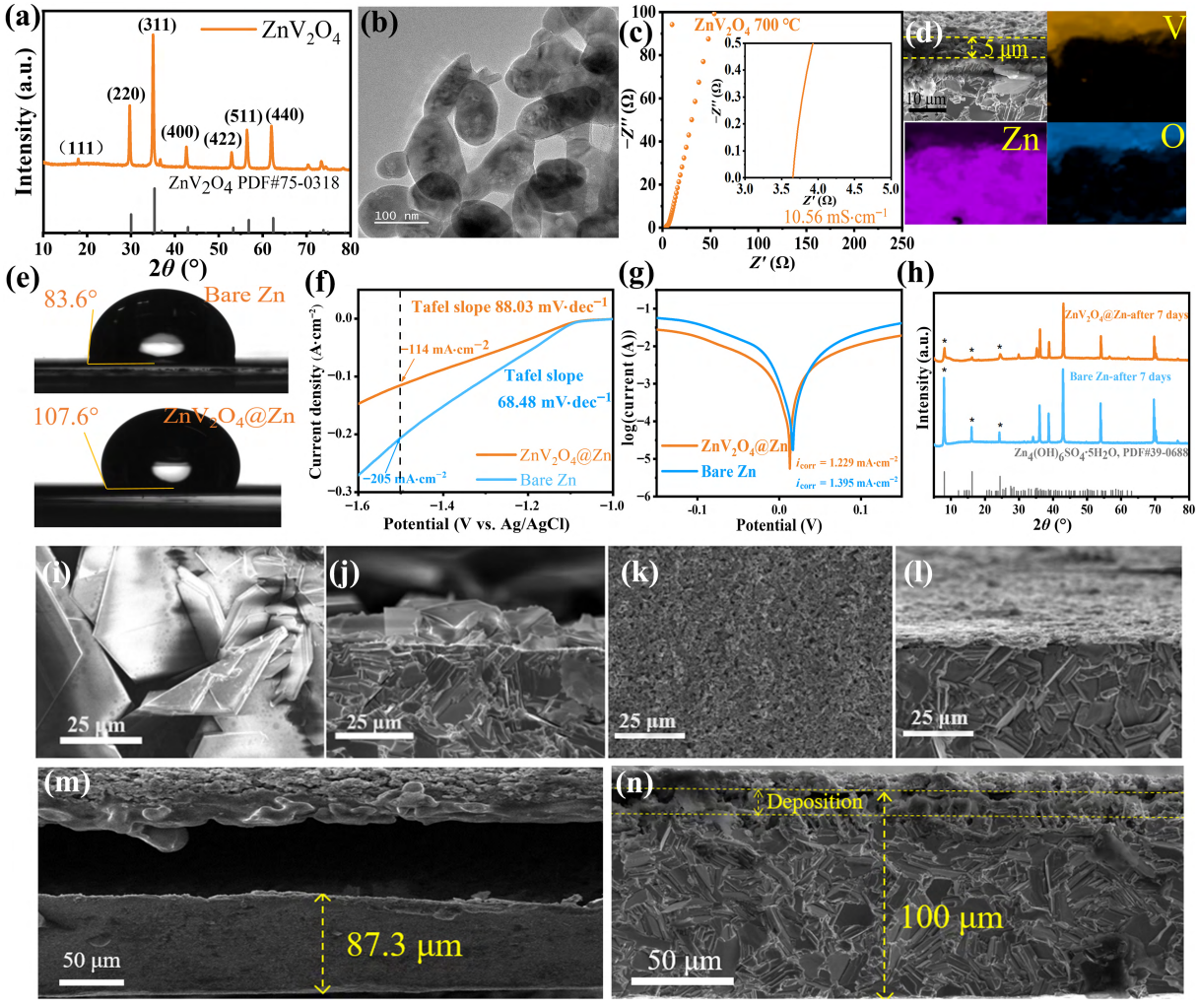

Figure 1 (a) XRD pattern of ZnV_2O_4. (b) The TEM image of ZnV_2O_4. (c) Ionic conductivity of ZnV_2O_4. (d) The thickness of the ZnV_2O_4@Zn electrode interface layer and the EDS mapping images of the cross-section. (e) Contact angle measurement on the electrode surface. (f) Electrochemical linear sweep voltammetry curves of hydrogen evolution and the corresponding Tafel curves. (g) Tafel plots of ZnV_2O_4@Zn and bare Zn. (h) The XRD patterns of bare Zn and ZnV_2O_4@Zn after 7 days of immersion in 2 M $ZnSO_4$. (i) Top-view and (j) side-view SEM images of the bare Zn after 7 days of immersion in 2 M $ZnSO_4$ electrolyte. (k) Top-view and (l) side-view SEM images of the ZnV_2O_4@Zn after 7 days of immersion in 2 M $ZnSO_4$ electrolyte. (m) SEM cross-sectional image of electrochemical dissolution for ZnV_2O_4@Zn at 10 mA·cm^{-2}. (n) SEM cross-sectional image of electrochemical deposition ZnV_2O_4@Zn at 1 mA·cm^{-2}.

It is crucial to assess the influence of the ZnV_2O_4@Zn interphase on Zn electrode kinetics, nucleation mechanism, and dendrite formation during electrodeposition. In Fig. 2(a), the ZnV_2O_4@Zn electrode exhibits a lower charge transfer resistance due to the high ionic conductivity of ZnV_2O_4, which facilitates rapid ion transport and diminishes concentration polarization. The cyclic voltammetry (CV) in Fig. 2(b) further shows that the nucleation overpotential for Zn plating/stripping on the ZnV_2O_4@Zn electrode (0.019 V) is lower than that on the bare Zn electrode (0.029 V). In Fig. 2(c), the exchange current density of the ZnV_2O_4@Zn anode (7.02 mA·cm^{-2} derived from Fig. S11 in the ESM) is higher than that of bare Zn (5.06 mA·cm^{-2}). This can be attributed to the ZnV_2O_4 interphase facilitating Zn^{2+} transport across the interface, thereby improving reaction kinetics and reversibility. Regarding the nucleation behavior on Zn plating process, Fig. 2(d) reveals that the initial nucleation overpotential of ZnV_2O_4@Zn is 48.7 mV, which is lower than the 60.3 mV for bare Zn. The chronoamperometry (CA) profile in Fig. 2(e) demonstrates that ZnV_2O_4@Zn undergoes a transition from two-dimensional (2D) to 3D diffusion-dominated growth more rapidly than bare Zn. Figures 2(f) and 2(g) compare the Zn^{2+} transference numbers, which clearly indicate that ZnV_2O_4@Zn interphase has a transference number more than three times that of the bare Zn anode (0.74 vs. 0.23). Even when used in 2 M $Zn(CF_3SO_3)_2$, ZnV_2O_4@Zn exhibits a Zn^{2+} transference number of 0.72 (Fig. S12 in the ESM). The close Zn^{2+} transference number further corroborates the preferential Zn^{2+} transport behavior induced by ZnV_2O_4 interface. We also contrast the X-ray photoelectron spectroscopy (XPS) spectra of ZnV_2O_4@Zn before and after 50 cycles (Fig. 2(h) and Fig. S13 in the ESM) to confirm its electrochemical stability. There are no noticeable changes in the valence state and atom ratio for V element attesting to the structural integrity of ZnV_2O_4. In addition, to elucidate the modulating effect of ZnV_2O_4@Zn interphases on Zn^{2+} deposition topography, we also investigated the SEM images of ZnV_2O_4@Zn before and after 50 cycles, and the XRD patterns after 50 cycles. As illustrated in Figs. S14 and S15 in the ESM, there was no significant change in the surface of ZnV_2O_4@Zn, whereas bare Zn anode shows many pits and protrusions entangled with the fiberglass. As evidenced by the XRD of Fig. S16 in the ESM, the characteristic peak intensity of by-product $Zn_4(OH)_6SO_4·5H_2O$ in the cycled ZnV_2O_4@Zn electrode is

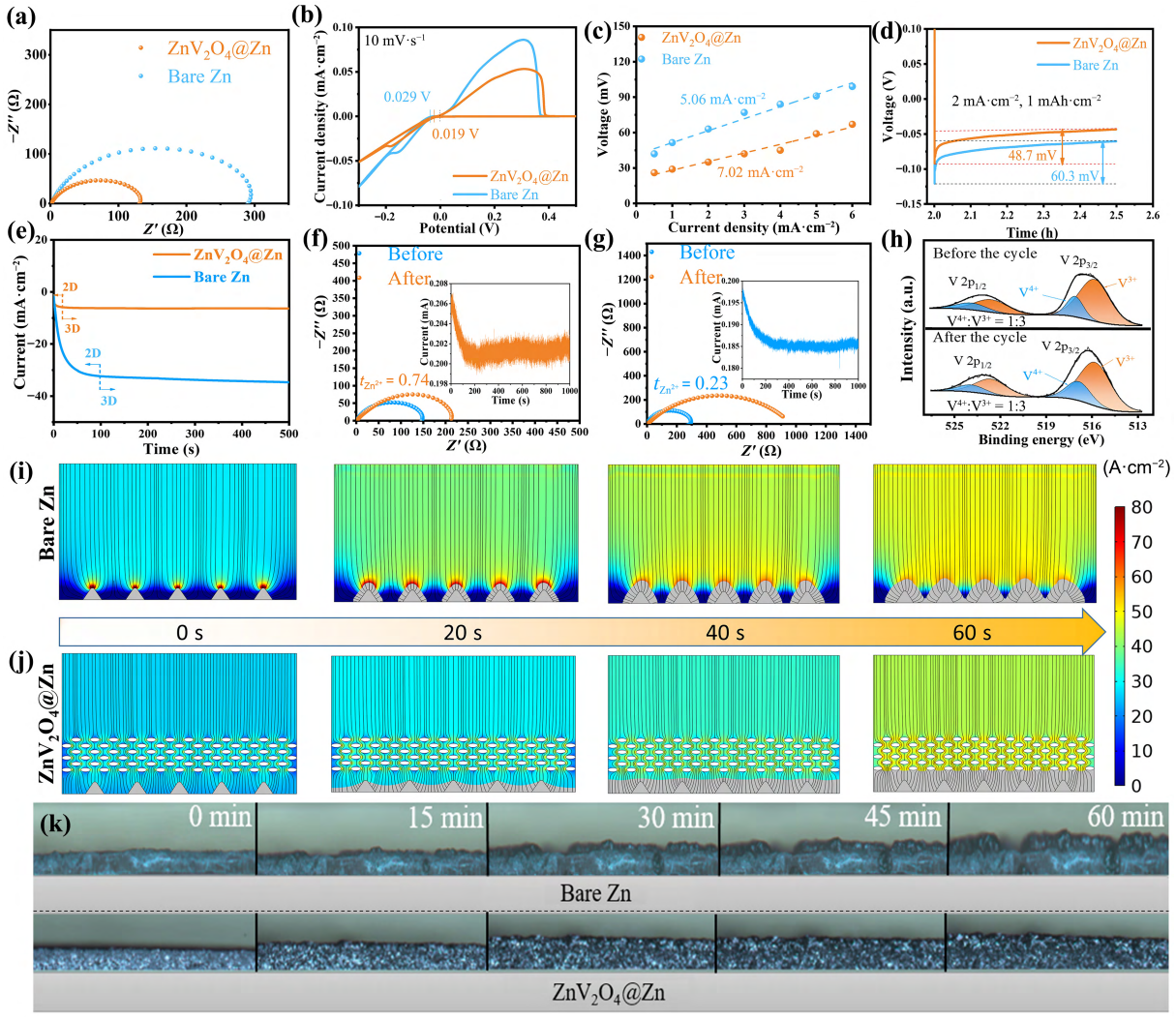

Figure 2 (a) EIS of bare Zn and ZnV_2O_4@Zn anodes. (b) CV curves of Zn//Cu and ZnV_2O_4@Zn//Cu half-cells. (c) Exchange current density of bare Zn and ZnV_2O_4@Zn anodes. (d) Nucleation overpotential of bare Zn and ZnV_2O_4@Zn electrodes at 2 mA·cm^{-2}. (e) Chronoamperometry test of symmetrical cells (−150 mV). (f) Zn^{2+} transference number of ZnV_2O_4@Zn. (g) Zn^{2+} transference number of bare Zn. (h) The XPS spectra of ZnV_2O_4@Zn before and after 50 cycles at 2 mA·cm^{-2}/1 mAh·cm^{-2}. The electric field distribution simulation for (i) bare Zn and (j) ZnV_2O_4@Zn electrodes. (k) *In situ* optical microscopy visualization of Zn plating on bare Zn and ZnV_2O_4@Zn electrodes at 10 mA·cm^{-2}.

markedly lower than that in bare Zn electrode, which confirms the excellent corrosion resistance of ZnV_2O_4 interphase again.

In order to further understand the evolution of the Zn deposition mechanism, electric field and ion field simulations are employed to compare the distribution conditions on bare Zn and ZnV_2O_4@Zn electrodes. With the time evolution, more uniform electric field for ZnV_2O_4@Zn electrode effectively mitigates the formation tendency of Zn dendrites. In contrast, the electric field around bare Zn readily attracts and accumulates Zn^{2+} ions, resulting in surface deposition irregularities and severe dendrite formation (Figs. 2(i) and 2(j)). The simulation of ion concentration distribution in Fig. S17 in the ESM also reveals more homogeneous Zn ion concentration distribution on ZnV_2O_4@Zn electrode than on the bare Zn electrode. Moreover, *in situ* optical visualization reveals a stark contrast; the ZnV_2O_4@Zn anode maintains a smooth, dendrite-free surface after 1 h of Zn plating, whereas on bare Zn, small protrusions emerge as early as 15 min and gradually evolve into severe dendrites (Fig. 2(k)).

To elucidate the relationship between surface structure and 3D tunnels for rapid ion transport, electron paramagnetic resonance (EPR) analysis is used to confirm the surface oxygen vacancy of ZnV_2O_4 ion sieve interface. As shown in Fig. 3(a) and Fig. S18 in the ESM, ZnV_2O_4 at 700 °C possesses the lowest amount of oxygen vacancies compared to that calcined at 500 and 600 °C, which can preserve the inner lattice integrity. Long-term cycling performance in Fig. S19 in the ESM also demonstrates that regular transport tunnels with moderate oxygen vacancies can afford the requirement of large rate performance. Except that, the moderate presence of oxygen vacancies in ZnV_2O_4 serves as Zn^{2+} adsorption sites, which can lower the diffusion energy barrier for high Zn^{2+} flux and further facilitate the desolvation of $[Zn(H_2O)_6]^{2+}$ [46–49]. Density functional theory (DFT) calculations in Fig. 3(b) further corroborate the atomic-scale insight into the Zn^{2+} adsorption. The calculated binding energy for Zn atoms adsorbed on the ZnV_2O_4 substrate is determined to be −1.368 eV, substantially lower than that on bare Zn substrate (−0.715 eV) and $ZnV_2O_4^0$ substrate (−1.0121 eV). The DFT result further theoretically indicates stronger attraction of ZnV_2O_4 interface toward Zn ion, which would benefit the Zn ion passage through the ion sieve interface.

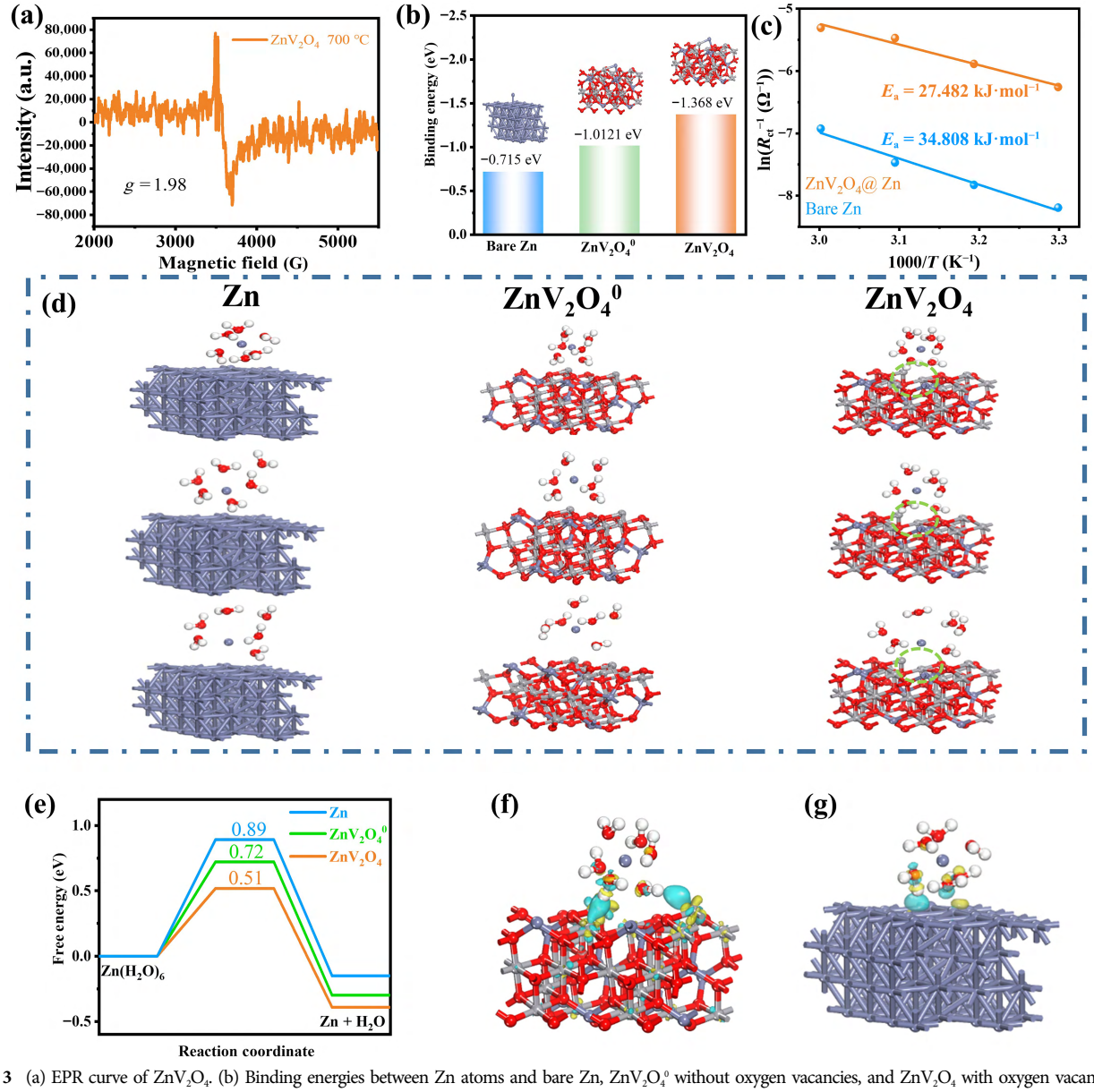

Figure 3 (a) EPR curve of ZnV_2O_4. (b) Binding energies between Zn atoms and bare Zn, $ZnV_2O_4^0$ without oxygen vacancies, and ZnV_2O_4 with oxygen vacancies. (c) Arrhenius curves and comparison of activation energies of different cells. (d) Molecular dynamics calculations for the desolvation process. (e) Energy barrier for taking off H_2O molecules from $[Zn(H_2O)_6]^{2+}$. The deformation charge density of (f) ZnV_2O_4@Zn and (g) bare Zn.

Figure 3(c) displays the linear correlation calculated between the reciprocal of temperature and the corresponding $\ln(R_{ct}^{-1})$ (where R_{ct} stands for charge-transfer resistance) for both ZnV_2O_4@Zn and bare Zn symmetric cells derived from the electrochemical impedance spectroscopy (EIS) measurements for Zn//Zn symmetric cells at 30, 40, 50, and 60 °C (Fig. S20 in the ESM). According to the Arrhenius equation, the activation energy (E_a) for the ZnV_2O_4@Zn symmetric cell is calculated to be 27.482 kJ·mol^{-1}, which is considerably lower than the value of 34.808 kJ·mol^{-1} obtained for the bare Zn symmetric cell. This marked decrease in activation energy confirms the role of ZnV_2O_4@Zn in facilitating the desolvation process, thereby inhibiting the coordination of H_2O molecules with dissolved Zn^{2+} ions. As shown in Figs. 3(d) and 3(e), molecular dynamics calculations are conducted on ZnV_2O_4, $ZnV_2O_4^0$ and bare Zn for the desolvation process. Calculation results reveal a markedly lower energy barrier for the desolvation of $[Zn(H_2O)_6]^{2+}$ on ZnV_2O_4 (0.51 eV) compared to that on $ZnV_2O_4^0$ (0.72 eV) and bare Zn (0.89 eV). As revealed by the differential charge density maps for ZnV_2O_4 (Fig. 3(f)), the Zn^{2+} on the surface of ZnV_2O_4 clearly undergoes electron rearrangement. Regions of electron accumulation (yellow) are localized around the adsorbed Zn^{2+} ions and specific surface sites of ZnV_2O_4, whereas electron depletion (blue) is observed in adjacent areas of the substrate. In contrast, the charge density around the bare Zn anode remained largely unchanged (Fig. 3(g)). This pronounced charge redistribution signifies a strong interaction between Zn^{2+} and the ZnV_2O_4 surface, which promotes uniform nucleation. Besides, the enhanced electron density at the interface further corroborates the increased adsorption energy.

After understanding that ZnV_2O_4@Zn interphases enhanced the Zn deposition process and prevented dendrite formation, we began to evaluate the performance of batteries using ZnV_2O_4@Zn to protect Zn as an anode. Zn//Cu asymmetric cells serve as a reliable method for evaluating the Coulombic efficiency and

electrochemical reversibility of Zn deposition/dissolution processes. Therefore, Zn//Cu asymmetric cells are tested. Notably, the ZnV_2O_4@Zn//Cu battery demonstrates excellent cycle stability within approximately 4000 cycles while maintaining a high average Coulombic efficiency of 99.77%. Conversely, the bare Zn//Cu battery fails rapidly after only 200 cycles (Fig. 4(a)).

This is primarily attributable to the accumulation of side-reaction products and dendritic Zn formations, which collectively impede efficient electron conduction and result in electrochemically inactive Zn. Comparably, the implementation of the ZnV_2O_4@Zn anode yields a significant decrease in electrode polarization, originating from a reduced activation energy barrier and enhanced Zn^{2+} ion transport kinetics. This synergistic effect guarantees a highly reversible and electrochemically stable cycling performance. In addition, the ZnV_2O_4@Zn//Cu battery initially shows a relatively low voltage hysteresis, maintaining a stable value of about 46 mV (Fig. S21 in the ESM), and it can also stabilize at 49 mV after 3000 cycles (Fig. 4(b)). In contrast, the bare Zn//Cu battery exhibits an initial voltage hysteresis as high as 121 mV, indicating significant polarization (Fig. S22 in the ESM). To evaluate the enhanced cycling stability enabled by the ZnV_2O_4@Zn, the Zn//Zn symmetric cells are tested. The ZnV_2O_4@Zn symmetric battery exhibits dramatically enhanced cycling stability across various current densities. Its lifespan reaches up to 1500 h at 2 mA·cm^{-2}/1 mAh·cm^{-2} and an impressive 3700 h at 4 mA·cm^{-2}/1 mAh·cm^{-2} (Fig. 4(c) and Fig. S23 in the ESM). Remarkably, even under a high current density of 8 mA·cm^{-2}, it sustains stable cycling for over 900 h (Fig. 4(d)). In stark contrast, bare Zn fails after only approximately 250 and 200 h at 2 and 4 mA·cm^{-2}, respectively. These findings offer further confirmation that the introduction of the ZnV_2O_4@Zn interphase markedly boosts symmetric battery performance. The ZnV_2O_4@Zn coating confers exceptional reversibility to Zn plating/stripping processes, outperforming the majority of previously documented protective coatings (Fig. 4(e)). Further, the rate capability of the symmetric cells is presented in Fig. 4(f). The ZnV_2O_4@Zn anode demonstrates smaller and more stable voltage hysteresis relative to the bare Zn anode across different current densities. As the current density is elevated from 0.5 to 8 mA·cm^{-2}, the bare Zn electrode shows a substantial increase in potential, suggestive of underlying instability and fluctuating current behavior. Conversely, the ZnV_2O_4@Zn electrode exhibits excellent voltage stability, underscoring its capability to reduce charge transfer resistance at the electrode–electrolyte interface and enhance Zn ion diffusion kinetics. Upon returning the current

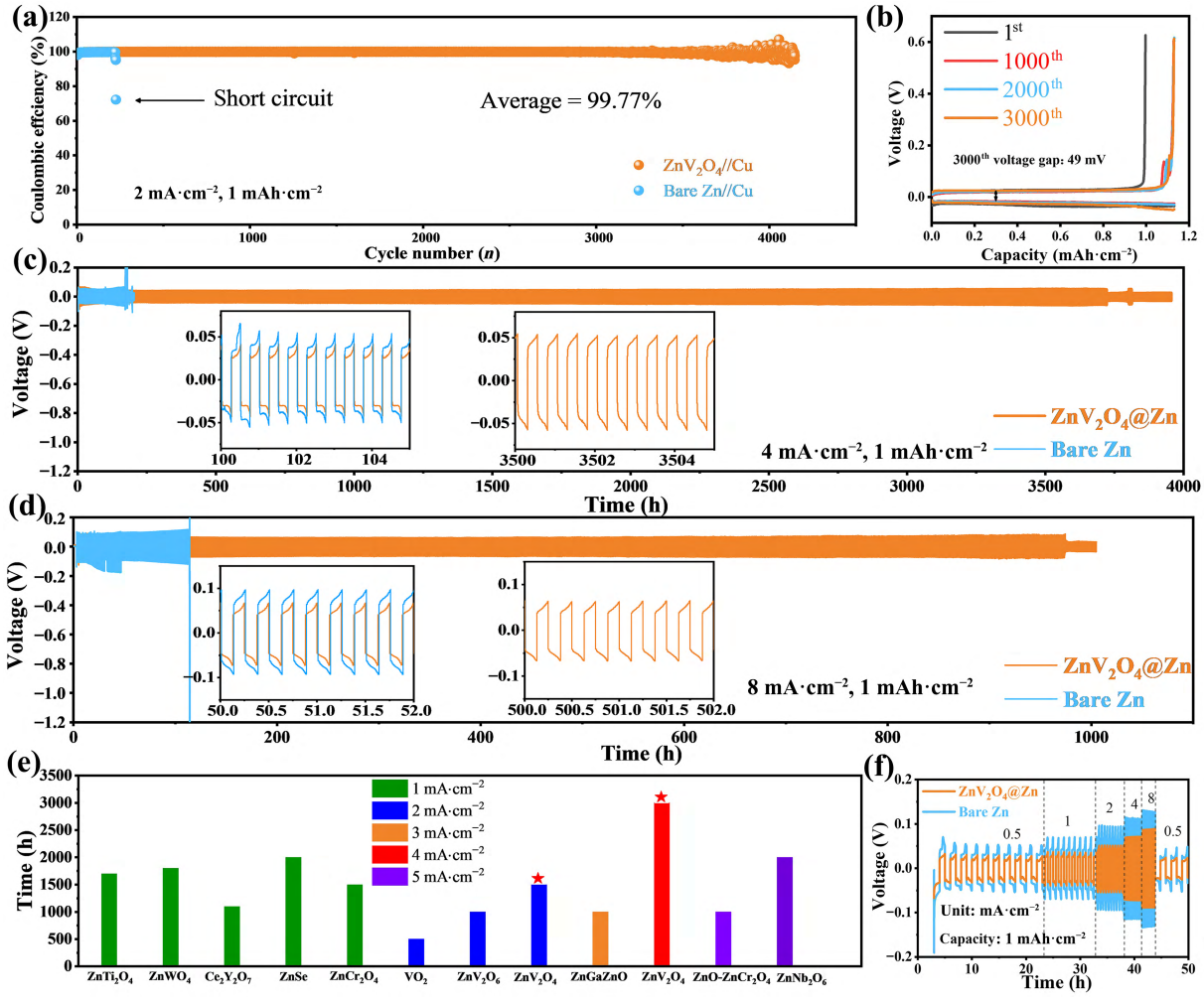

Figure 4 (a) Coulombic efficiency performance of Zn//Cu half cell. (b) The ZnV_2O_4@Zn anode over different numbers of cycles. (c) Cycling performance of bare Zn and ZnV_2O_4@Zn symmetric cells at 4 mA·cm^{-2}/1 mAh·cm^{-2}. (d) Cycling performance of bare Zn and ZnV_2O_4@Zn symmetric cells at 8 mA·cm^{-2}/1 mAh·cm^{-2}. (e) Comparison of the cycle life of symmetric cells between this work and other reports. (f) The rate performances of the symmetric cells at various current densities under a fixed capacity of 1 mAh·cm^{-2}.

density to 0.5 mA·cm^{-2}, the ZnV_2O_4@Zn anode still maintains a relatively low voltage hysteresis, demonstrating its exceptional electrochemical reversibility and cycling stability. These investigations underscore that the ZnV_2O_4@Zn interphases enable superior electrochemical stability and sustain cycling performance for Zn-ion aqueous batteries.

The superiority of ZnV_2O_4@Zn is further verified in a Zn//δ-MnO_2 full cell. Figures S24 and S25 in the ESM present the XRD pattern and the SEM image of the as-synthesized δ-MnO_2, respectively. As depicted in Fig. 5(a), both ZnV_2O_4@Zn//MnO_2 and bare Zn//MnO_2 full cells display nearly identical cyclic voltammetry profiles, indicating that the energy storage mechanism of the cathode material is not affected by ZnV_2O_4@Zn. The ZnV_2O_4@Zn//MnO_2 full cell demonstrates a narrower voltage separation between redox peaks, suggesting that ZnV_2O_4@Zn improves the charge transfer kinetics. Next, the rate capabilities of both full cells are investigated from 0.2 to 5 A·g^{-1} (Fig. 5(b)). The cell with ZnV_2O_4@Zn demonstrates consistently higher capacity than that with bare Zn. This improved rate capability is attributed to the reduced charge transfer resistance enabled by the ZnV_2O_4@Zn coating, as quantitatively demonstrated in Fig. 5(c). The ZnV_2O_4@Zn//MnO_2 full cell exhibits not only enhanced rate capability but also remarkable cycling durability. As depicted in Fig. 5(d), the ZnV_2O_4@Zn//MnO_2 full cell maintains a capacity of 200 mAh·g^{-1} after 1000 cycles, with a capacity retention of 52.5%. This performance markedly surpasses that of the bare Zn//MnO_2 full cell (70.2 mAh·g^{-1}). Figure 5(e) presents the galvanostatic charge/discharge curves of ZnV_2O_4@Zn//MnO_2 and bare Zn//MnO_2 cells at 1 A·g^{-1}. The ZnV_2O_4@Zn//MnO_2 cell exhibits significantly reduced voltage polarization compared to the unmodified bare Zn//MnO_2 system. As demonstrated in Figs. 5(f) and 5(g), the ZnV_2O_4@Zn//MnO_2 full cell achieves a higher retention rate of 99.81%, whereas bare Zn//MnO_2 battery exhibits a capacity retention of 97.68% after a 24 h charged stand period under identical conditions, which further confirms the feasibility of ZnV_2O_4 ion sieve interphase to stabilize Zn metal anodes.

3 Conclusions

In summary, the spinel-type ZnV_2O_4 ion sieve interface with moderate oxygen vacancies and the inner interconnected tunnels was engineered on the Zn anode, which synergistically integrates the strong zincophilic nature of oxygen vacancies and excellent ion selectivity, enabling high Zn ion flux and intensive desolvation. The moderate oxygen vacancies afford abundant affinity sites for Zn^{2+} and ensure the lattice integrity of the inner interconnected three-dimensional tunnel. The suitable tunnel size selectively facilitates the rapid and homogeneous transport of Zn^{2+}. It not only significantly enables uniform Zn deposition but also promotes the desolvation process of hydrated Zn^{2+} ions. Benefitting from the unique ion sieve interface, the assembled ZnV_2O_4@Zn symmetric

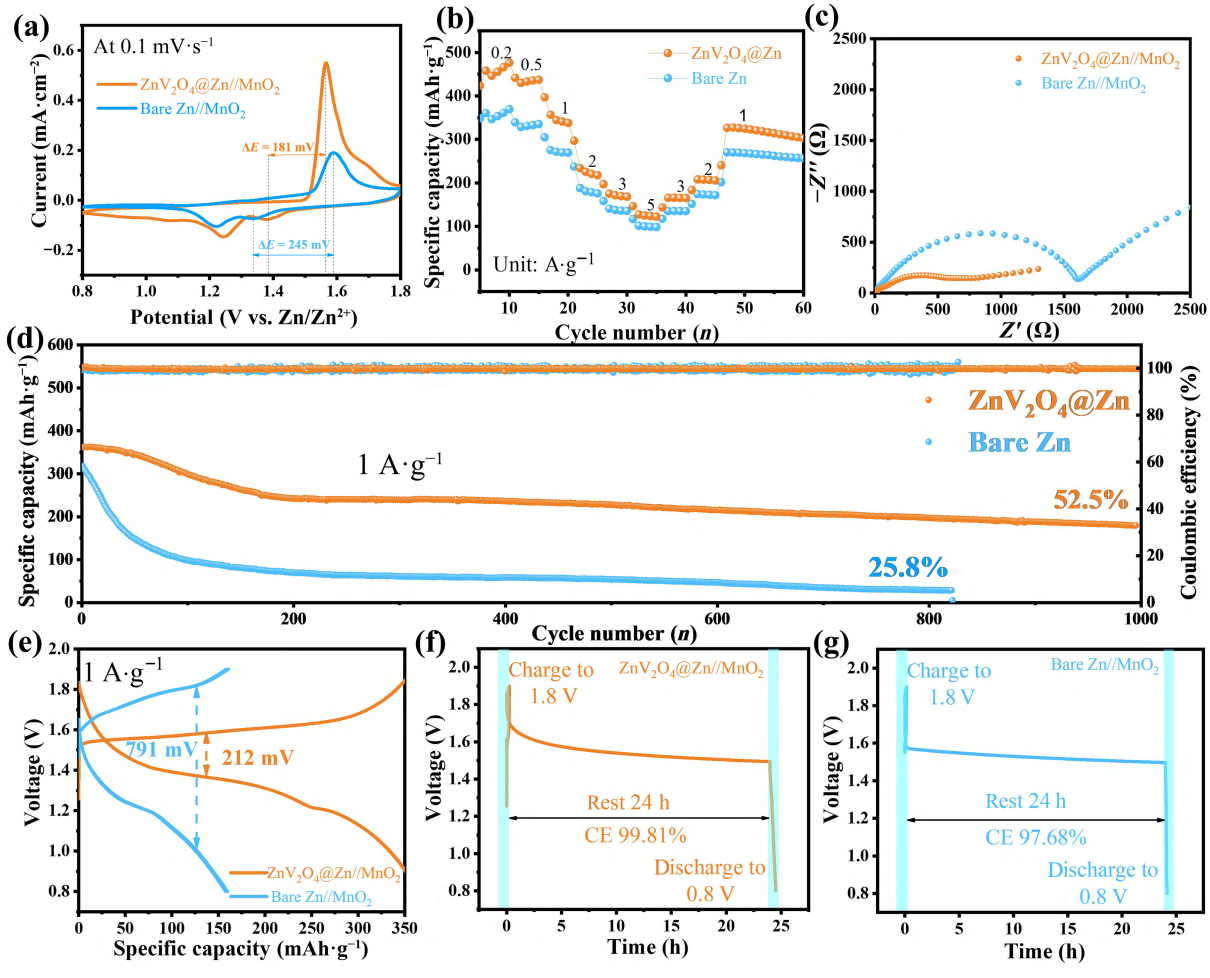

Figure 5 Electrochemical performances of Zn//MnO_2 full cells with bare Zn and ZnV_2O_4@Zn anodes. (a) CV curves at 0.1 mV·s^{-1}. (b) Rate performance and (c) EIS curves. (d) Cycling performance at 1 A·g^{-1}. (e) The charge–discharge curves. ((f) and (g)) Self-discharge curves.

cell delivers an ultra-stable cycling lifespan of 3700 h at 4 mA·cm^{-2}/1 mAh·cm^{-2}. In Zn//MnO_2 full cells, this work demonstrates a generalizable strategy based on the synergistic combination of high ion flux and selectivity, offering a promising avenue for durable aqueous batteries.

Electronic Supplementary Material: Supplementary material (further details of materials synthesis and battery assemble, electrochemical measurements, computational method, SEM images, XRD patterns, EDS mapping images, and COMSOL simulations) is available in the online version of this article at https://doi.org/10.26599/NR.2026.94908542.

Data availability

All data needed to support the conclusions in the paper are presented in the manuscript and the Electronic Supplementary Material. Additional data related to this paper may be requested from the corresponding author upon request.

Acknowledgements

This work is financially supported by the National Natural Science Foundation of China (No. 22362010), Innovation Research team project of Guangxi Province (No. 2023GXNSFGA026002), and Guangxi Technology Base and Talent Subject (No. GUIKE AD25069022).

Declaration of competing interest

All the contributing authors report no conflict of interests in this work.

Author contribution statement

B. L. L.: Data curation, validation, writing manuscript, experimental design. G. X. Z.: Data curation. Y. X. L.: Visualization. L. W.: Visualization. Y. X. Z.: Visualization. H. Q. W.: Funding acquisition. Q. Y. L.: Funding acquisition. Z. L. M.: Project administration, writing – review & editing, funding acquisition. All the authors have approved the final manuscript.

Use of AI statement

None.

References

[1] Hu, N.; Lv, W. S.; Chen, W. J.; Tang, H.; Zhang, X. Y.; Qin, H. Y.; Huang, D.; Zhu, J. L.; Chen, Z. J.; Xu, J. et al. A double-charged organic molecule additive to customize electric double layer for super-stable and deep-rechargeable Zn metal pouch batteries. *Adv. Funct. Mater.* **2024**, *34*, 2311773.

[2] Liu, Z. P.; Xu, G. N.; Zhang, Y.; Li, M.; Li, H. R.; Zhang, J. C.; Hu, J.; Lin, T. S.; Zhang, N. Q. Unveiling zinc stripping and molecular engineering for high-performance zinc anode. *Angew. Chem.* **2025**, *137*, e202501960.

[3] Bian, H. F.; Li, C. C.; Xue, G.; Wu, H.; Wang, B.; Li, F. Q.; Bin, D.; Lu, H. B.; Meng, X. K. Smart self-healing anode/electrolyte interphases for stabilizing Zn anode. *Adv. Mater.* **2025**, *37*, 2505982.

[4] Gomez Vazquez, D.; Tabor, J.; Pollard, T. P.; Borodin, O.; Lukatskaya, M. R. Measuring Zn transference with precision: Insights for dendrite-free zinc metal anodes. *Adv. Mater.* **2025**, *37*, e02245.

[5] Tang, S.; Wei, Q. Y.; Liu, B. Q.; Yang, J. L.; Jiang, H. Z.; Ge, Y. Z.; Wu, D. X.; Li, J.; Qiu, T. Y.; Zhang, H. et al. Simultaneous manipulation of electric double layer and Zn (100) deposition enabled by anions for highly stable Zn anodes. *Angew. Chem., Int. Ed.* **2025**, *64*, e202510252.

[6] Nguyen, V. P.; Park, M.; Byeon, Y. W.; Lim, S.; Yim, K.; Oh, M.; Hyun, S.; Jeon, E. C.; Lee, S. M. Ultrathin yet effective: 90 nm ZnF_2 layer for stabilizing zinc-metal anodes. *ACS Energy Lett.* **2025**, *10*, 5503–5511.

[7] Su, T. T.; Ren, W. F.; Xu, M.; Xu, P. W.; Le, J. B.; Ji, X.; Dou, H. Z.; Sun, R. C.; Chen, Z. W. *In situ* construction of bionic self-recognition layer for high-performance zinc-iodine batteries. *Adv. Energy Mater.* **2024**, *14*, 2401737.

[8] Yang, T. Y.; Su, T. T.; Wang, H. L.; Li, K.; Ren, W. F.; Sun, R. C. "Tennis racket" hydrogel electrolytes to synchronously regulate cathode and anode of zinc-iodine batteries. *J. Energy Chem.* **2025**, *102*, 454–462.

[9] Song, Y.; Liu, Y. D.; Luo, S. J.; Yang, Y. R.; Chen, F. D.; Wang, M.; Guo, L.; Chen, S. G.; Wei, Z. D. Blocking the dendrite-growth of Zn anode by constructing Ti_4O_7 interfacial layer in aqueous Zinc-ion batteries. *Adv. Funct. Mater.* **2024**, *34*, 2316070.

[10] Rong, D.; Zou, S. J.; Wu, Y.; He, S. J.; Rong, Q. F. Electric field-induced gradient polyanionic hydrogel electrolytes with zinc-ion selective transport for stable zinc-ion batteries. *Chem. Eng. J.* **2025**, *524*, 169746.

[11] Liang, H. H.; Ji, H. M.; Huang, X. Z.; Li, Y. X.; Xu, Y.; Hu, C.; Xu, Y. Z.; Zhang, Q.; Li, H. H.; Tang, Y. G. et al. Electronic structure and lattice vibration regulating enables highly stable Zn metal anode for zinc ion batteries. *Adv. Funct. Mater.* **2026**, *36*, e18044.

[12] Nie, C. H.; Wang, G. L.; Wang, D. D.; Wang, M. Y.; Gao, X. R.; Bai, Z. C.; Wang, N. N.; Yang, J.; Xing, Z.; Dou, S. X. Recent progress on Zn anodes for advanced aqueous zinc-ion batteries. *Adv. Energy Mater.* **2023**, *13*, 2300606.

[13] Yang, M.; Zhang, Y. N.; Li, Q. J.; Wang, X.; Ma, B. Y.; Niu, Z. Q. The design of interfacial organic-riched phase by molecular interlocking for stable Zn anodes. *Angew. Chem., Int. Ed.* **2025**, *64*, e202512032.

[14] Liu, W.; Zhao, Q. W.; He, S. R.; Yu, H. M.; Li, Y.; Cao, P. H.; Kuang, G. C.; Xu, B. G.; Chen, Y. J.; Chen, L. B. Sustainable release of zincophilic metal ions from separator proactively drives interfacial stabilization for durable zinc anode. *Adv. Funct. Mater.* **2025**, *35*, 2425680.

[15] Dong, Z. X.; Zhong, C. K.; Chai, H.; Weng, G.; Chen, J.; Guo, X. Y.; Wang, Y. K.; Jiang, J. L.; Huang, X. L.; Fan, J. C. et al. Emerging *in situ* thermal treatment strategies for tailoring uniform Zn deposition toward stable Zn anodes. *Adv. Funct. Mater.* **2025**, *35*, 2503502.

[16] Zhang, B. W.; Qian, T. Y.; Li, R. M.; Chen, J. P.; Zhang, X.; Zhao, W. Y.; Zhang, J. L.; Yuan, Y. X.; Ma, Z. F.; Yang, X. W. Terminating interfacial hydrogen-bond networks via preferential coordination for stable zinc metal anode. *J. Energy Chem.* **2025**, *107*, 1–8.

[17] Fu, K.; Wang, H. J.; Xie, M. L.; Zhang, Y. Q.; Xin, Y. X.; Xu, X. W.; Wu, Y. R.; Li, Z. D.; Luo, Y. D.; Ma, Y. C. et al. Self-assembly of super-hydrophobic and zincophilic surface monolayer for durable Zn anodes. *Energy Storage Mater.* **2025**, *78*, 104281.

[18] Elshahawy, A. M.; Gao, Y.; Zhao, W. B.; Li, J. W.; Zhang, H. F.; Liu, X. M. Hygroscopic organic complex mutated helmholtz plane of Zn anode for outstanding zinc ion battery. *Energy Environ. Mater.*, in press, DOI: 10.1002/eem2.70151.

[19] Su, T. T.; Ren, W. F.; Xu, M.; Li, K.; Yang, T. Y.; Wang, D. D.; Dou, H. Z.; Sun, R. C.; Chen, Z. W. A reusable biomass electrolyte with dual-interface regulation towards flexible and durable zinc-iodine batteries. *Energy Storage Mater.* **2025**, *78*, 104279.

[20] Xiao, Y.; Wang, T.; Su, T. M.; Tang, S. C.; Xiang, W. W.; Shaik, J. A.; Yu, J. S. Interface engineering with electrospun zincophilic-hydrophobic architecture for robust Zn metal anodes. *J. Energy Chem.* **2026**, *113*, 669–678.

[21] Chen, Z. Y.; Zhao, Y. F.; Cui, P.; Zhu, J. Y.; Gao, X.; He, G. J.; Yi, X. S. Unidirectional ion sieve enabling high-flux and reversible zinc anodes. *ACS Nano* **2025**, *19*, 14987–15001.
[22] Zhu, R. Y.; Ren, X.; Wu, L.; Tian, L. Y.; Zhang, H.; Meng, Y. W.; Zhou, J. Enabling targeted zinc growth via interface regulation toward binder free and high areal capacity zinc metal anode. *Adv. Mater.* **2025**, *37*, 2503516.
[23] Feng, D. D.; Jiao, Y. C.; Wu, P. Y. Proton-reservoir hydrogel electrolyte for long-term cycling Zn/PANI batteries in wide temperature range. *Angew. Chem.* **2023**, *135*, e202215060.
[24] Zhou, L. J.; Wang, F. X.; Yang, F.; Liu, X. Q.; Yu, Y. X.; Zheng, D. Z.; Lu, X. H. Unshared pair electrons of zincophilic lewis base enable long-life Zn anodes under "three high" conditions. *Angew. Chem., Int. Ed.* **2022**, *61*, e202208051.
[25] Wang, W. K.; Yang, C.; Chi, X. W.; Liu, J. H.; Wen, B.; Liu, Y. Ultralow-water-activity electrolyte endows vanadium-based zinc-ion batteries with durable lifespan exceeding 30 000 cycles. *Energy Storage Mater.* **2022**, *53*, 774–782.
[26] Liu, D. R.; Wang, Z.; Zhao, D.; Guo, S. J.; Zhang, L. Z. Y.; Luo, Y. Z.; Cao, F. F. Design strategies and advanced methods for cathode engineering in aqueous zinc-iodine batteries. *Small Methods* **2025**, *9*, e01287.
[27] Yang, J. J.; Zhao, R.; Wang, Y. S.; Hu, Z. F.; Wang, Y. H.; Zhang, A. Q.; Wu, C.; Bai, Y. Insights on artificial interphases of Zn and electrolyte: Protection mechanisms, constructing techniques, applicability, and prospective. *Adv. Funct. Mater.* **2023**, *33*, 2213510.
[28] Wu, F. F.; Chen, Y. C.; Chen, Y. L.; Yin, R. L.; Feng, Y. C.; Zheng, D.; Xu, X. L.; Shi, W. H.; Liu, W. X.; Cao, X. H. Achieving highly reversible zinc anodes via N,N-dimethylacetamide enabled Zn-ion solvation regulation. *Small* **2022**, *18*, 2202363.
[29] Zeng, X. H.; Mao, J. F.; Hao, J. N.; Liu, J. T.; Liu, S. L.; Wang, Z. J.; Wang, Y. Y.; Zhang, S. L.; Zheng, T.; Liu, J. W. et al. Electrolyte design for *in situ* construction of highly Zn^{2+}-conductive solid electrolyte interphase to enable high-performance aqueous Zn-ion batteries under practical conditions. *Adv. Mater.* **2021**, *33*, 2007416.
[30] Yang, T. Y.; Su, T. T.; Xu, M.; Wang, D. D.; Ren, W. F.; Dou, H. Z.; Sun, R. C.; Chen, Z. W. Dienoic-acid coupling effect induced hierarchical interface for high-performance zinc metal batteries. *Angew. Chem., Int. Ed.* **2025**, *64*, e202512780.
[31] Yan, H. B.; Han, C.; Li, S. M.; Liu, J. H.; Ren, J.; Yang, S. B.; Li, B. Adjusting zinc ion de-solvation kinetics via rich electron-donating artificial SEI towards high columbic efficiency and stable Zn metal anode. *Chem. Eng. J.* **2022**, *442*, 136081.
[32] Wang, J. X.; Zhang, H.; Yang, L. Z.; Zhang, S. Y.; Han, X. P.; Hu, W. B. *In situ* implanting 3D carbon network reinforced zinc composite by powder metallurgy for highly reversible Zn-based battery anodes. *Angew. Chem., Int. Ed.* **2024**, *63*, e202318149.
[33] Wang, T. Q.; Tang, Y.; Yu, M. X.; Lu, B. G.; Zhang, X. T.; Zhou, J. Spirally grown zinc-cobalt alloy layer enables highly reversible zinc metal anodes. *Adv. Funct. Mater.* **2023**, *33*, 2306101.
[34] Liu, W.; Zhao, Q. W.; Yu, H. M.; Wang, H.; Huang, S. Z.; Zhou, L. J.; Wei, W. F.; Zhang, Q. C.; Ji, X. B.; Chen, Y. J. et al. Metallic particles-induced surface reconstruction enabling highly durable zinc metal anode. *Adv. Funct. Mater.* **2023**, *33*, 2302661.
[35] Fang, Y. T.; Lei, P. C.; Xing, H. R.; Cai, W. L.; Fan, Z. C.; Wang, W. W.; Wu, Q. Y.; Wu, X. J.; Zhu, Y. C. Quinone carbonyl activation for *in situ* constructing kinetic-boosted zincophilic polymer interphase toward high performance Zn metal anode. *Energy Storage Mater.* **2024**, *65*, 103097.
[36] Liu, X.; Ma, Q. X.; Shi, M. D.; Han, Q. G.; Liu, C. G. A biomimetic polymer-clay nanocomposite coating for dendrite-free Zn metal anode. *Chem. Eng. J.* **2023**, *456*, 141016.
[37] Amer, A. A.; Zhu, Q. Z.; Xu, M. Y.; Tunesi, M. M.; Xu, B. Optimized nitrogen sites in yolk–shell ZnNCN/nitrogen-doped carbon composite interfacial layer for dendrite-free and highly reversible Zn anodes. *Small* **2025**, *21*, 2505128.
[38] Wang, Y.; Liu, Y. N.; Wang, H. Q.; Dou, S. M.; Gan, W.; Ci, L. J.; Huang, Y.; Yuan, Q. H. MOF-based ionic sieve interphase for regulated Zn^{2+} flux toward dendrite-free aqueous zinc-ion batteries. *J. Mater. Chem. A* **2022**, *10*, 4366–4375.
[39] Zhang, K.; Li, C. X.; Liu, J. W.; Zhang, S. H.; Wang, M. H.; Wang, L. Defect-rich functional HfO_{2-x} for highly reversible Zn metal anode. *Small* **2024**, *20*, 2306406.
[40] Chen, Y. H.; Lyu, F. C.; Guan, Z. Z.; Zhou, L.; Xie, Y. N.; Long, Y. C.; Shen, J. D.; Yu, H. Y.; Miao, M. L.; Mao, Z. Y. et al. Engineering low-coordination atoms into $Zn_2Ti_3O_8$ for stable Zn metal anodes. *Adv. Funct. Mater.* **2026**, *36*, e08468.
[41] Shi, Z. H.; Chen, S. L.; Xu, Z. J.; Liu, Z. M.; Guo, J. H.; Yin, J.; Xu, P. W.; Zhang, N.; Zhang, W. L.; Alshareef, H. N. et al. Metal oxide aerogels: A new horizon for stabilizing anodes in rechargeable zinc metal batteries. *Adv. Energy Mater.* **2023**, *13*, 2300331.
[42] Shen, S. C.; Ma, D. T.; Ouyang, K. F.; Chen, Y. W.; Yang, M.; Wang, Y. Y.; Sun, S. C.; Mi, H. W.; Sun, L. N.; He, C. X. et al. An *in situ* electrochemical amorphization electrode enables high-power high-cryogenic capacity aqueous zinc-ion batteries. *Adv. Funct. Mater.* **2023**, *33*, 2304255.
[43] Luo, B.; Wang, Y.; Zheng, S. N.; Sun, L. L.; Duan, G. S.; Bao, Z. A.; Ye, Z. Z.; Huang, J. Y. High-capacity spatial confined deposition/stripping enabled by biphasic modulation strategy for highly reversible zinc anodes. *Energy Storage Mater.* **2024**, *71*, 103661.
[44] Huang, M. C.; Zhao, X. Y.; Hu, Y. J.; Lei, Y. J.; Liu, C. Y.; Zhai, S. L. Ion-sieving nanolayers for highly reversible zinc-ion batteries. *Chem. Eng. J.* **2025**, *522*, 167433.
[45] Sun, J.; Jian, Q. P.; Liu, B.; Lin, P. Z.; Zhao, T. S. *In situ* growth of 2D metal–organic framework ion sieve interphase for reversible zinc anodes. *Energy Environ. Mater.* **2024**, *7*, e12769.
[46] Wang, W. R.; Li, Z. P.; Li, W. X.; Jin, Q. F.; Gao, J. B.; Zhao, J. X.; Liang, Q. C.; Zhang, B. Q.; Xie, H. J.; Chen, P. CeY bimetallic oxide coating with abundant oxygen vacancies and superior semiconductor property for the stable zinc metal anode. *Chem. Eng. J.* **2025**, *512*, 162304.
[47] Wang, T.; Xu, L. L.; Xiang, W. W.; Tang, S. C.; Xiao, Y.; Yu, J. S. Interfacial lattice strain-induced vacancy evolution facilitating highly reversible dendrite-free zinc metal anodes. *Adv. Energy Mater.* **2024**, *14*, 2402586.
[48] Wang, J. J.; Hou, S. Y.; Huang, C.; Liu, T. Z.; Shi, T. F.; Wang, X.; Hou, S.; Zhao, L. Z. Regulating amorphous structure and mechanical strength induce enhanced interface chemistry toward long-life rechargeable aqueous Zn-ion batteries. *J. Energy Chem.* **2025**, *105*, 617–629.
[49] Xu, M. Z.; He, X. Y.; Xue, S. J.; Xiao, X.; Wang, J. Y.; Meng, S.; Xu, Q.; Chen, Z. F. Unveiling ion pairing reorganization mechanism of oxygen vacancy-rich amorphous molybdenum oxide-based solid-electrolyte interphase for fast Zn^{2+} desolvation. *Adv. Energy Mater.* **2026**, *16*, e03167.